

## Chapter

# Ferromagnetism in Multiferroic BaTiO<sub>3</sub>, Spinel MFe<sub>2</sub>O<sub>4</sub> (M = Mn, Co, Ni, Zn) Ferrite and DMS ZnO Nanostructures

*Kuldeep Chand Verma, Ashish Sharma, Navdeep Goyal  
and Ravinder Kumar Kotnala*

## Abstract

Multiferroic magnetoelectric material has significance for new design nano-scale spintronic devices. In single-phase multiferroic BaTiO<sub>3</sub>, the magnetism occurs with doping of transition metals, TM ions, which has partially filled d-orbitals. Interestingly, the magnetic ordering is strongly related with oxygen vacancies, and thus, it is thought to be a source of ferromagnetism of TM:BaTiO<sub>3</sub>. The nanostructural MFe<sub>2</sub>O<sub>4</sub> (M = Mn, Co, Ni, Cu, Zn, etc.) ferrite has an inverse spinel structure, for which M<sup>2+</sup> ions in octahedral site and Fe<sup>3+</sup> ions are equally distributed between tetrahedral and octahedral sites. These antiparallel sublattices (cations M<sup>2+</sup> and Fe<sup>3+</sup> occupy either tetrahedral or octahedral sites) are coupled with O<sub>2-</sub> ion due to superexchange interaction to form ferrimagnetic structure. Moreover, the future spintronic technologies using diluted magnetic semiconductors, DMS materials might have realized ferromagnetic origin. A simultaneous doping from TM and rare earth ions in ZnO nanoparticles could increase the antiferromagnetic ordering to achieve high-T<sub>c</sub> ferromagnetism. The role of the oxygen vacancies as the dominant defects in doped ZnO that must involve bound magnetic polarons as the origin of ferromagnetism.

**Keywords:** magnetically ordered material, oxygen vacancies, spin glass

## 1. Introduction

Multiferroics are combining multiple order parameters, offer an exciting way of coupling phenomena such as electronic and magnetic order. However, because simultaneous electric and magnetic order is difficult to achieve, multiferroics—especially those that function at or approaching room temperature—are extremely rare. For a crystal, when electrons are surrounded atomic nuclei to orient themselves in a same fashion then the crystal induces macroscopic ferromagnetism and electrical polarization. Since induction of ferromagnetism is essential in the technologies that involved sensors, computer hard drives, power generation, etc. Recently, the diluted magnetic semiconductors (DMSs) such as ZnO, SnO<sub>2</sub>, TiO<sub>2</sub>, etc. have generated potential in spintronics because DMS has the collective ordering that mediated via semiconductor charge carriers, as well as electron scattering

at localized magnetic impurities and electron–electron interactions. To use DMSs for practical spintronic devices, a relatively high concentration of magnetic elements needed in the semiconductor host, and a large ferromagnetism is required with a Curie temperature ( $T_c$ ) above room temperature. The transition metal (TM) ferrites with a spinel structure ( $MFe_2O_4$ ;  $M = Co^{2+}, Ni^{2+}, Cu^{2+}, Zn^{2+}$ , etc.) are used in a wide variety of technological applications such as magnetic memory devices and biomedicine. However, these spinel ferrites are the candidate materials for multiferroic heterostructure due to their excellent magnetic response. For such multiferroic heterostructures, the perovskite ( $BaTiO_3$ ,  $PbTiO_3$ ,  $BiFeO_3$ , etc.) has an opportunity of higher piezoelectric coefficient that may pool with magnetostrictive materials ( $CoFe_2O_4$ ,  $NiFe_2O_4$ ,  $ZnFe_2O_4$ , etc.) via lattice strain effect.

### 1.1 Multiferroic $BaTiO_3$

The magnetoelectric (ME) effect—the induction of magnetization by an electric field and the induction of electric polarization by a magnetic field [1]. Multiferroic nanostructures have given recent advances in new type of memory devices including multistate data storage and spintronics [2].  $BaTiO_3$  (BTO) is a rare single-phase multiferroic. In multiferroics, the magnetic order is due to exchange interactions between magnetic dipoles, which themselves originate from unfilled shells of electron orbitals. Similarly, the electric order is due to the ordering of local electric dipoles, elastic order is due to the ordering of atomic displacements due to strain. The three crystallographic phases of BTO are ferroelectric: rhombohedral  $<190$  K, orthorhombic for  $190$  K  $< T < 278$  K and tetragonal for  $278$  K  $< T < 395$  K. At higher temperatures, BTO is a paraelectric. For tetragonal BTO (**Figure 1(b)**) having lattice constants:  $a(\text{Å}) = b(\text{Å}) = 3.99$ ;  $c(\text{Å}) = 4.03$ ; space group =  $P4mm$ , the displacement of  $Ti^{4+}$  ion along  $c$ -axis might be induced electrical polarization (ferroelectricity). It involved hybridization of charge among Ti cation (3d states) with O anions (2p states). In cubic phase, the  $Ba^{2+}$  is located at the centre of the cube with coordination number 12.

Since to the formation of ME random access memories (MERAMs), the main thing that required ME coupling via interfacial exchange coupling among a multiferroic and a ferromagnet, which can change the magnetization of the ferromagnetic coating with respect to a voltage (**Figure 1(a)**) [3]. For such MERAMs, an electric field is enabled by ME coupling could control the exchange coupling between multiferroic and ferromagnetic at the interface. This exchange coupling at the interface reins the magnetization of the ferromagnetic layer, and therefore the magnetization might be change with multiferroic electrical polarization. Therefore, for perovskite ( $ABO_3$ ) BTO,  $Ba^{2+}$  (A-site cation) induce the required distortion for ferroelectricity, while magnetism can be achieved by the doping such as TM = Cr, Mn, Fe, Co, Ni, Cu along B-site cation [4, 5].

### 1.2 Spinel ferrites

The spinel structure typically represented as  $AB_2O_4$ , where ‘A’ indicates four-fold coordinated tetrahedral sub-lattice sites and ‘B’ indicates six-fold coordinated octahedral sub-lattice (**Figure 1(c)**). There are 8 A-sites in which the metal cations are tetrahedrally coordinated with oxygen, and 16 B-sites, which possess octahedral coordination. Normal ferrites have divalent cations residing solely as the central ion on the tetrahedral sub-lattice with only trivalent Fe cations occupying octahedral sub-lattice sites. Harrisa and Sepelak [6] suggested superexchange interaction, the  $J_{BB}$  is strong and negative indicating antiferromagnetic coupling between  $Fe^{3+}-O^{2-}-Fe^{3+}$  with octahedral sub-lattice cation spins largely canceling out. When

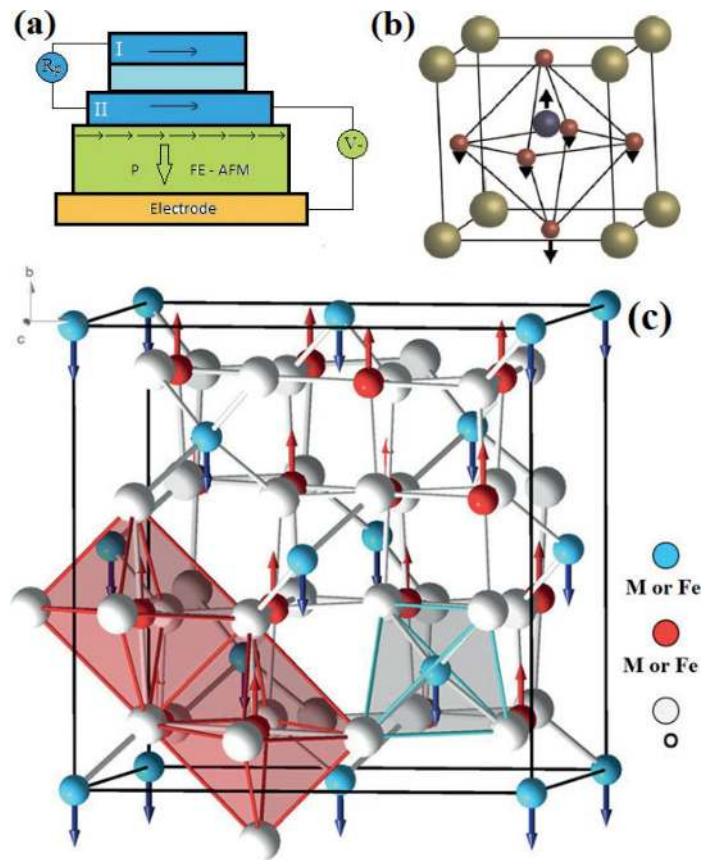


**Figure 1.** (a) Schematic MERAM device in which the binary information is stored by the magnetization direction of the ferromagnetic layer (I & II), read by the resistance,  $R_p$  of the magnetic trilayer, and written by applying a voltage across the multiferroic ferroelectric-antiferromagnetic layer (FE-AFM). (b) Tetragonal crystalline structure of BTO, with a lattice ferroelectric distortion. (c) Spinel unit cell. Arrows represent magnetic moments and their antiparallel alignment. Adopted from Harrisa and Sepelak [6].

the divalent cation resides on the [B] site and A and B ions share the balance of [B] and the totality of (A), the spinel is inverse:  $(A_{1-\delta}B_\delta)[A_\delta B_{2-\delta}]O_4$ , where  $\delta$  is the inversion degree, *i.e.*, NiFe<sub>2</sub>O<sub>4</sub>. Ferrite of the type NiFe<sub>2</sub>O<sub>4</sub> (NFO), CoFe<sub>2</sub>O<sub>4</sub> (CFO) and MnFe<sub>2</sub>O<sub>4</sub> (MFO) with the spinel structure are magnetic ceramics which have potential in electronic and magnetic components [7]. The NFO has an inverse spinel structure for which Fe<sup>3+</sup> ions occupied tetrahedral A-sites; whereas Fe<sup>3+</sup> and Ni<sup>2+</sup> ions are sit on octahedral B-sites. This NFO is ferrimagnetic material has magnetization originated by antiparallel spins on A- and B-sites. However, for normal spinel structure of CFO, Co is a divalent atom, occupying tetrahedral A-sites, while Fe is a trivalent atom, sitting on the octahedral B-sites. For MFO, the inverted spinel structure is partial for which the Mn<sup>2+</sup> and Fe<sup>3+</sup> ions with half-filled 3d shell (ground state is singlet <sup>6</sup>S with spin = 5/2 with zero orbital momentum) and the crystal field is not sufficient to split it [8]. The magnetic moment of MFO agrees well with Neel's coupling scheme and has lower resistivity than CFO and NFO ferrites [9].

### 1.3 Diluted magnetic semiconductors

Recently, the realization of spin in DMS, semiconductor with substituted magnetic impurities (Fe, Co, Ni, Cu) has attracted great interest in design of spintronics devices like spin field-effect transistors, non-volatile memory devices, and programmable logic gates [10–13]. Among various DMS, ZnO is a promising spin

source, since it epitomizes DMS with  $T_c$  well above room temperature. The DMS ZnO is a wide band gap that gained recent research in spintronics, due to an ability to change its optical and magnetic behavior with doping of TM = Fe, Co, Mn, Ni, Cu, Cr, or V ions and/or by intrinsic defects, such as oxygen vacancy ( $V_O$ ) and zinc vacancy ( $V_{Zn}$ ). The DMS ZnO has wide applications included:

### 1.3.1 Magnetic recording

For read heads in magnetic disk recorders (computer components), read head senses the magnetic bits that are stored on the media, which is stored as magnetized regions of the media, called magnetic domains, along tracks (**Figure 2(a)**) [13]. Magnetization is stored as a “0” in one direction and as a “1” in the other. Although, there is no magnetic field emanating from the interior of a magnetized domain itself, uncompensated magnetic poles in the vicinity of the domain walls generate magnetic fields (sensed by the GMR element) that extend out of the media.

### 1.3.2 Nonvolatile memories

The “Nonvolatile” refers to information storage that does not “evaporate” when power is removed from a system, *i.e.*, magnetic disks and tapes. Prinz [13] has recently demonstrated that GMR elements can be fabricate in arrays with standard lithographic processes to obtain memory that has speed and density approaching that of semiconductor memory, but is nonvolatile. A schematic representation of RAM that is constructed of GMR elements is shown in **Figure 2(b)**. The spin-dependent scattering of the carriers (electrons & holes) is minimized for parallel magnetic moment of the ferromagnetic layer, to induce lowest value of resistance. However, the highest resistance is the result of maximized spin-dependent scattering carriers via anti-aligned ferromagnetic layers. An external magnetic field could give the direction of magnetic moments, applied to the materials. The spin-valve structures of GMR set into series using lithographic (wires) termed as a sense line. This sense line has information storage due to resistance (resistance of elements). The sense line runs the current which is detected at the end by amplifiers because resistance changes in the elements.

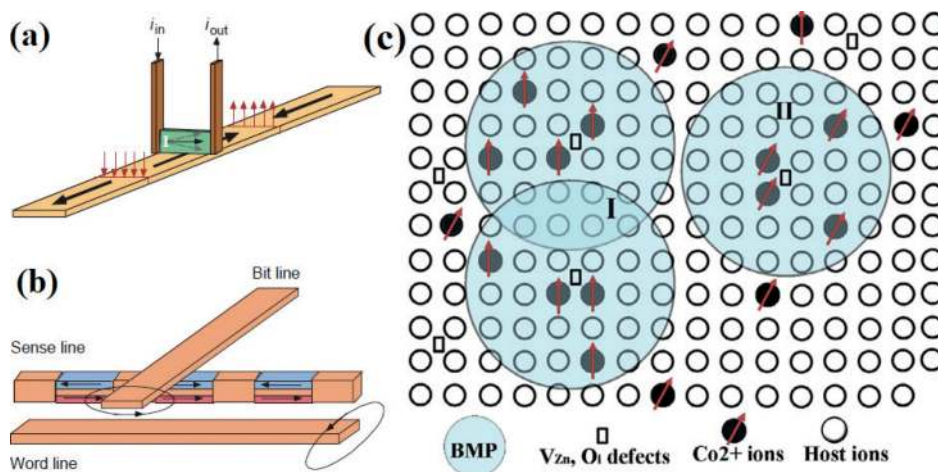


**Figure 2.** A schematic representation of (a) GMR read head ( $I$ ) that passes over recording media containing magnetized regions, (b) RAM that is constructed of GMR elements. Adopted from Prinz [13], (c) bound magnetic polaron (BMP),  $V_{Zn}$ ,  $O_i$  trapped carriers couple with the 3d shell spins of TM ions within its hydrogenic orbit.

### 1.3.3 Ferromagnetism in DMS ZnO due to bound magnetic polarons

Generally, the room temperature ferromagnetism (RTFM) in DMS ZnO is given because of bound magnetic polaron (BMP) model [14]. The localized spins of the dopant ion interact with the charge carriers that are bound to a small number of defects such as oxygen vacancies, resulting into a magnetic polarization of the surrounding local moments. Since the magnetism in TM ions doped ZnO nanoparticles relates with exchange interactions between unpaired electron spins, that arising from the lattice imperfections such as oxygen vacancies, V<sub>O</sub> at the surface of the nanoparticles. Pal et al. [15] described BMP formation in Co doped ZnO and shown in **Figure 2(c)**. The electrons trapped in the defect vacancies undergo orbital coupling with the *d* shells of the adjacent divalent dopant ion and form BMP. In BMP model, the bound electrons (holes) hold in defect states that coupled through TM ions to overlap ferromagnetic regions, which responsible into high T<sub>C</sub> (due to formation of long-range ferromagnetic ordering) [16]. When the dopant ions are donors or acceptors, the exchange interactions are sp-d that would lead BMPs formation.

## 2. Experimental methods

The multiferroic, DMS and ferrites materials might be synthesized by methods such as a sol-gel [17], chemical combustion [18], hydrothermal [19], metallo-organic decomposition (MOD) [20], conventional solid-state reaction [21], sol-gel precipitation [22], thermal evaporation [23], etc.

## 3. Result and discussion

### 3.1 Multiferroic systems of BaTiO<sub>3</sub>

#### 3.1.1 X-ray diffraction for BaTiO<sub>3</sub> and BaTM<sub>0.01</sub>Ti<sub>0.99</sub>O<sub>3</sub> nanoparticles

The sol-gel method is used to prepare pure BaTiO<sub>3</sub> and BaTM<sub>0.01</sub>Ti<sub>0.99</sub>O [TM = Cr (BTO:Cr), Mn (BTO:Mn), Fe (BTO:Fe), Co (BTO:Co), Ni (BTO:Ni), Cu (BTO:Cu)] nanoparticles [4]. The TM ions in perovskite BTO structure highly influenced lattice constants to induce lattice strain and unit cell expansion, which responsible into defects vacancies formation. **Figure 3** shows the Rietveld refinement (Full-Prof program) of X-ray diffraction (XRD) patterns for pure and BaTM<sub>0.01</sub>Ti<sub>0.99</sub>O nanoparticles measured at room temperature. A polycrystalline with tetragonal BTO phase (space group: P4mm) is detected. The fitting parameters, R<sub>p</sub>(%) = 6.7, 7.1, 6.7, 4.9, 9.1, 8.2 and 9.8, R<sub>wp</sub>(%) = 3.2, 9.9, 9.2, 10.0, 12.5, 1.2 and 14.6,  $\chi^2$  = 1.1, 1.4, 0.81, 1.4, 3.3, 3.3 and 0.9 and distortion ratio, (*c/a*) = 1.00959, 1.00932, 1.00688, 1.00909, 1.00776, 1.00625 and 1.00508, respectively, refined for pure BTO and BTO with Cr, Mn, Fe, Co, Ni, Cu doping. Also, **Figure 3(a)** shows the tetragonal splitting of (200) diffraction peak at 2 $\theta$  = 44.3–45.7°. The diffraction peak of pure BTO has shifted towards a lower diffraction angle with TM doping which supports the lattice strain in BTO. Such splitting of (200) peak might be confirmed the tetragonal phase formation. It is due to electrostatic repulsions between 3d electrons of Ti<sup>4+</sup> ions and 2p electrons of O<sup>2-</sup> ions, the structure becomes distorted. It is also reported in Ref. [4] that the average particles size, from TEM, D<sub>TEM</sub> (nm) = 20 ± 3, 13 ± 1, 33 ± 5, 35 ± 3, 17 ± 1 and 47 ± 7, the value of saturation magnetization, M<sub>s</sub> (emu g<sup>-1</sup>) = 0.056, 0.042, 0.066, 0.035, 0.013 and 0.021, and the ME coupling constant,  $\alpha_{ME}$  (mV cm<sup>-1</sup> Oe<sup>-1</sup>) = 25.91, 11.27, 31.15, 16.58, 11.61 and 16.48, respectively, measured with Cr, Mn, Fe, Co, Ni, Cu doping into BTO.

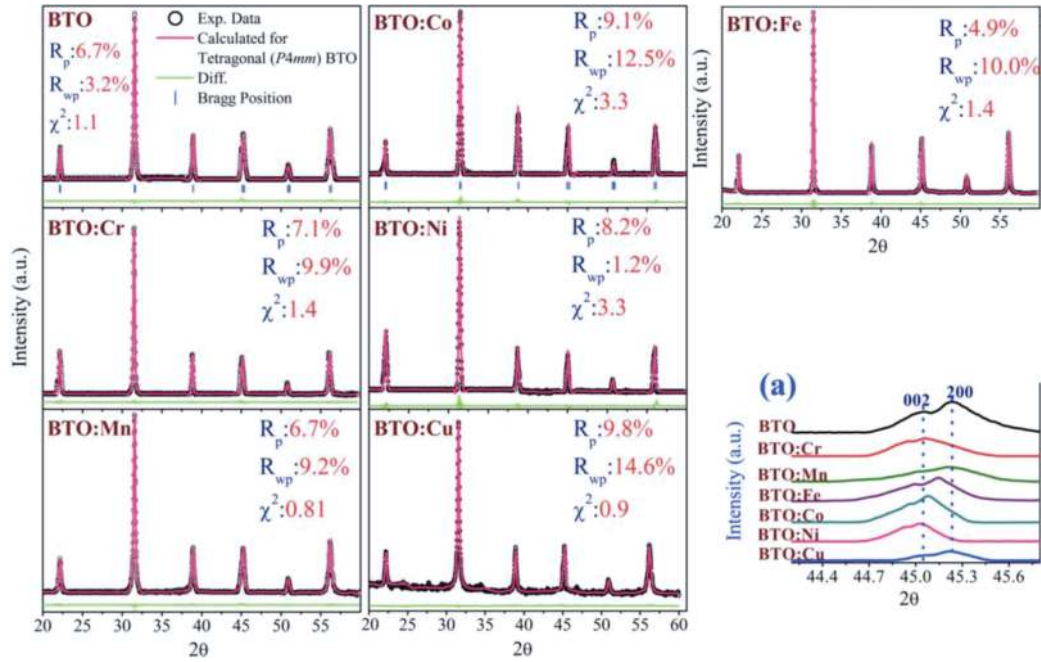


**Figure 3.** XRD pattern for pure  $\text{BaTiO}_3$  and  $\text{BaTM}_{0.01}\text{Ti}_{0.99}\text{O}_3$  nanoparticles. (a) Showing the splitting of the (200) peak. Adapted from Verma and Kotnala [4].

### 3.1.2 Nanostructure of $\text{BaTiO}_3$ (BTO) and $\text{BaFe}_{0.01}\text{Ti}_{0.99}\text{O}_3$ (BFTO) multiferroic

The BTO and BFTO were prepared by a hydrothermal method of processing temperature  $180^\circ\text{C}/48\text{ h}$  [5]. The XRD pattern shows the coexistence of cubic/tetragonal/hexagonal phases of BTO and cubic/tetragonal of BFTO. **Figure 4(a and b)** reveals the TEM images of BTO and BFTO nanostructure. It shown that BTO (**Figure 4(a)**) is the product that consist of nanorods structure having hexagonal like face of average diameter 50 nm and length 75 nm. However, **Figure 4(b)** shows the nanowires formation of BFTO with average diameter  $\sim 45\text{ nm}$  and the length  $>1.5\ \mu\text{m}$ . It is also reported in Ref. [5] that the room temperature  $M$ - $H$  hysteresis shows diamagnetism in BTO and ferromagnetism in BFTO with  $M_s \sim 82.23\text{ memu g}^{-1}$ ,  $M_r \sim 31.91\text{ memu g}^{-1}$  with  $H_c \sim 122.68\text{ Oe}$  and ME coupling coefficient,  $\alpha_{\text{ME}} = 16\text{ mV Oe}^{-1}\text{ cm}^{-1}$ .

### 3.1.3 Ferromagnetism/ferroelectricity in $\text{Ce,L a}:\text{BaFe}_{0.01}\text{Ti}_{0.99}\text{O}_3$ nanostructures

The nano-aggregation type  $\text{Ba}(\text{Fe}_{0.67}\text{Ce}_{0.33})_{0.01}\text{Ti}_{0.99}\text{O}_3$  (BFTO:Ce) and  $\text{Ba}(\text{Fe}_{0.67}\text{La}_{0.33})_{0.01}\text{Ti}_{0.99}\text{O}_3$  (BFTO:La) product is synthesized by a hydrothermal process [2]. Rietveld refinement of XRD pattern indicates polycrystalline phase with tetragonal BFTO. It is reported that the Ce and La ions in BFTO improved lattice distortion,  $c/a$  ratio. These dopant Ce and La in BFTO forms nano-aggregation type product with average value of aggregation diameter,  $D = 40$  and  $22\text{ nm}$ , respectively, for BFTO:Ce and BFTO:La. The formation of tetragonal BTO phase and lattice defects due to vacancies is attributed by Raman active modes. These defects and vacancies are also confirmed with photoluminescence measurement that might be altered due to higher surface-to-volume ratio in nano-aggregation. **Figure 4(d and e)** shows the ferromagnetic behavior of Ce, La doped BFTO, respectively, by magnetization versus field ( $M$ - $H_{\text{dc}}$  hysteresis) measured at room temperature [2]. The values of  $M_s$  ( $\text{emu g}^{-1}$ ) = 0.15 and 0.08, and  $M_r$  ( $\text{emu g}^{-1}$ ) = 0.039 and 0.015 with  $H_c$  (Oe) = 242 and 201, respectively, for BFTO:Ce and BFTO:La. It is well predicted that the formation of  $\text{Fe}^{4+}-\text{O}^{2-}-\text{Fe}^{4+}$  interaction is ferromagnetic, which dominate in BFTO over the antiferromagnetic  $\text{Fe}^{3+}-\text{O}^{2-}-\text{Fe}^{4+}$

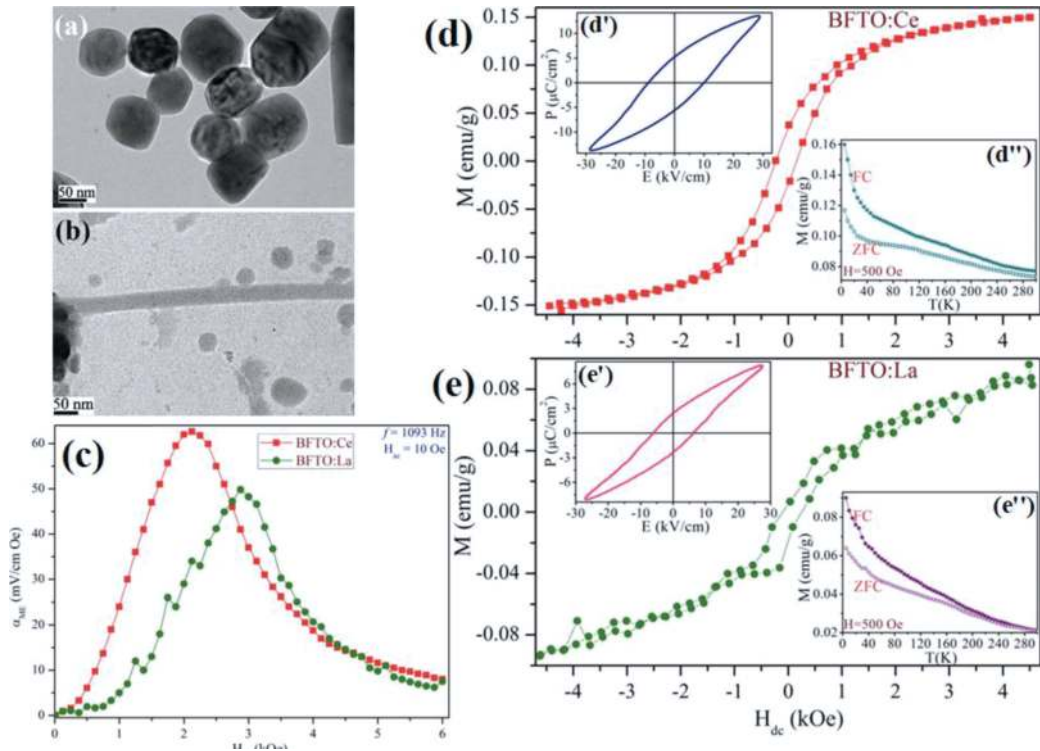


**Figure 4.** Transmission electron microscopy (TEM) of (a) pure BaTiO<sub>3</sub> (b) Ba(Fe<sub>0.01</sub>Ti<sub>0.99</sub>)O<sub>3</sub>, (c) ME voltage coefficient ( $\alpha_{ME}$ ), (d and e)  $M$ - $H_{dc}$  hysteresis at room temperature, (d' and e')  $P$ - $E$  hysteresis, and (d'' and e'')  $M(T)$  following ZFC/FC at  $H = 500$  Oe for Ce, La doped BFTO. Adopted from Refs. [2, 5].

and  $Fe^{3+}-O^{2-}-Fe^{3+}$  interactions, producing weak ferromagnetism. Generally, the ferromagnetism in Fe-doped BaTiO<sub>3</sub> is explained into two ways: the partially filled inner shells (d- or f-levels) and formation of nanostructures. An F-centre exchange (FCE) mechanism describes the required ferromagnetism [24, 25]. Such a mechanism expects  $Fe^{3+}-V_O^{2-}-Fe^{3+}$  transition that generally exists in the structure where an electron trapped in oxygen vacancies,  $V_O$  to form F-centre. For this, the electron occupies an orbital,  $p_z$  that overlaps  $d_z^2$  of d shells in iron neighbors. The  $Fe^{3+}$  ions have  $3d^5$  electronic configurations for which spin down trapped electron and spin up in two iron neighbors. Therefore, the F-centre has the exchange interaction among two iron ions that would leads to ferromagnetism. The insets of **Figure 4**(d' and e') show the polarization-electric field ( $P$ - $E$ ) hysteresis at room temperature. With Ce doping into BFTO, the value of spontaneous polarization,  $P_s$  ( $\mu C cm^{-2}$ ) = 13.83 and remanent polarization,  $P_r$  ( $\mu C cm^{-2}$ ) = 5.45 with electric coercivity,  $E_c$  ( $kV cm^{-1}$ ) = 9.53. However, with La doping,  $P_s$  ( $\mu C cm^{-2}$ ) = 8.28, and  $P_r$  ( $\mu C cm^{-2}$ ) = 2.46, with  $E_c$  ( $kV cm^{-1}$ ) = 6.14. These values of polarization have an improvement over reported work [26–28]. This is due to nano-aggregation formation and lattice distortion enhancement in BTO lattice. The smaller polarization in BFTO:La is the nano-size effect that involved compensation of polarization-induced surface charges [29].

### 3.1.4 Magnetization at low temperature measurement

The origin of observed ferromagnetism at room temperature in Ce- and La-doped BFTO is described by measuring their magnetization from zero-field cooling (ZFC) and field cooling (FC) at 500 Oe (**Figure 4**(d'' and e'')). A clear separation between FC and ZFC retains up to low temperature without blocking temperature is observed. This is an indication of weak antiferromagnetic interactions.

An upward curvature observed in M-T curve suggests a Curie-Weiss like behavior. It is attributed with short-range ferromagnetism, or a spin-cluster within a matrix of spin disorder [30]. Li et al. [31] suggested that the oxygen vacancy might be mediate antiferromagnetic-ferromagnetic interactions in multiferroics.

### 3.1.5 ME coupling in Ce, La-substituted BFTO

The longitudinal ME coupling coefficient,  $\alpha_{ME}$  is measured for Ce and La-doped BFTO and shown in **Figure 4(c)**. The samples are biased with *ac* magnetizing field,  $H_{ac} = 10$  Oe at 1093 Hz, and a *dc* magnetic field,  $H_{dc}$  is applied collinear to it. The value of  $\alpha_{ME}$  was determined as a function of *dc* magnetic field using:  $\alpha_{ME} = \frac{\partial E}{\partial H} = \frac{1}{t} \frac{\partial V}{\partial H} = \frac{V_{out}}{t \times H_{ac}}$ . In **Figure 4(c)**, the value of  $\alpha_{ME}$  increases rapidly to a maximal value (due to an enhancement of elastic interactions) and then slowly decreasing in the higher region of  $H_{dc}$ . The maximum value of  $\alpha_{ME}$  ( $\text{mV cm}^{-1} \text{Oe}^{-1}$ ) is 62.65 and 49.79, respectively, for BFTO:Ce and BFTO:La.

## 3.2 Spinel ferrites $M\text{Fe}_2\text{O}_4$ ( $M = \text{Mn, Co, Ni, Zn, Cu, etc.}$ )

### 3.2.1 Structural studies of $\text{Co}_{0.65}\text{Zn}_{0.35}\text{Fe}_2\text{O}_4$

**Figure 5 (a)** shows the Rietveld refinement (space group:  $Fd\bar{3}m$ ) of  $\text{Co}_{0.65}\text{Zn}_{0.35}\text{Fe}_2\text{O}_4$  (CZFO) ferrite, which indicate spinel phase [32]. The value of  $\chi^2$  is 1.648. The lattice parameter of CZFO is found to be 8.4183 Å. A three-dimensional sketch of CZFO unit cell projected along the *c*-axis (**Figure 5(b)**). The inset of **Figure 5(a)** shows the SEM image of a CZFO pellet sample to displays densely packed grains with few scattered pores and voids. It is also reported in Ref. [32] that the high dielectric permittivity value is obtained. The ferrimagnetic-paramagnetic phase transition is  $\sim 640$  K.

### 3.2.2 Lattice constant, grains size and magnetism in pure NFO, CFO and MFO thin films

**Table 1** shows the experimental results of lattice constant (*a*), grain's size [*x* (SEM) & *x'* (AFM)],  $M_s$ ,  $M_r$  and  $H_c$  measured at room temperature (300 K) and 10 K, and magnetic phase transition temperature ( $T_{pm}$ ) of  $\text{NiFe}_2\text{O}_4$  (NFO),

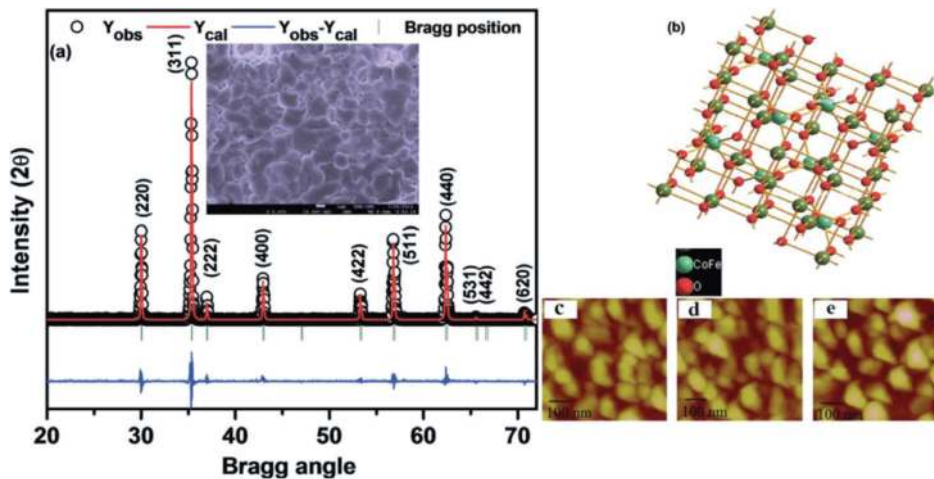


**Figure 5.** (a) XRD patterns and SEM image (inset) of  $\text{Co}_{0.65}\text{Zn}_{0.35}\text{Fe}_2\text{O}_4$  (CZFO). (b) CZFO unit cell with a spinel structure. AFM of (c) NFO, (d) CFO (e) MFO thin films. Adopted from Refs. [9, 32].



Sample	a (Å)	x (nm)	x' (nm)	M <sub>s</sub> (emu cc <sup>-1</sup> )			M <sub>r</sub> (emu cc <sup>-1</sup> )			H <sub>c</sub> (Oe)			T <sub>pm</sub> (K)
				300 K	10 K	300 K	10 K	300 K	10 K	300 K	10 K		
NFO	8.161	44	46	50.60	76.42	14.33	63.31	265.33	73.90	687			
CFO	8.312	60	61	33.50	54.57	15.50	8.90	1292.00	69.33	693			
MFO	8.425	74	75	5.40	13.35	1.10	7.20	113.30	39.28	581			

Adopted from Verma et al. [9].

**Table 1.**

Values of lattice constant (a), grain's size (x) (SEM), grain's size (x') (AFM), M<sub>s</sub>, M<sub>r</sub> and H<sub>c</sub> at 300 K and 10 K, and magnetic phase transition (T<sub>pm</sub>) of pure NFO, CFO and MFO thin films.

CoFe<sub>2</sub>O<sub>4</sub> (CFO) and MnFe<sub>2</sub>O<sub>4</sub> (MFO) thin films [9]. These ferrites were prepared by a MOD method using spin coating. The thickness of all the film is ~700 nm. It is also reported that the miller indices of cubic spinel ferrites structure are (2 2 0), (3 1 1), (2 2 2), (4 0 0), (3 3 1), (4 2 2) and (5 1 1), respectively, detected with diffraction angle  $2\theta = 30.48, 34.99, 37.48, 42.58, 48.02, 51.23$  and  $55.85^\circ$  for NFO, for CFO,  $2\theta = 30.25, 34.87, 37.36, 42.58, 47.20, 51.23$  and  $55.84^\circ$  and  $2\theta = 29.77, 34.64, 37.36, 41.75, 47.08, 51.23$  and  $57.04^\circ$  for MFO. The higher coercivity value of CFO than NFO and MFO is the effect of higher magneto-crystalline anisotropy of Co cations than Ni and Mn. The observed values of  $M_s$ ,  $M_r$  and  $H_c$  of the NFO, CFO and MFO films are quite smaller than bulk form [9]. For this, the decrease in  $M_s$  in ferrite nanoparticles is the canted spins in the surface layers [33]. Also, it observed very smaller values of  $M_r$ ,  $M_s$  and  $H_c$  of MFO because lowering number of magnetic domains and the rate of alignment of the spins with the applied field [34, 35].

### 3.2.3 AFM images of NFO, CFO and MFO thin films

The value of average grain's size from AFM (**Figure 5(c–e)**) is 46, 61 and 75 nm, and the surface roughness 2.5, 4 and 2 nm, respectively, for NFO, CFO and MFO ferrite thin films, were synthesized by MOD method [9].

### 3.2.4 Magnetic ordering of ferrites in MFe<sub>2</sub>O<sub>4</sub>/BaTiO<sub>3</sub> nanocomposite

The multiferroic MFe<sub>2</sub>O<sub>4</sub>/BaTiO<sub>3</sub> (MFO/BTO) thin films were fabricated by a MOD method [20]. The addition of ferrite MFe<sub>2</sub>O<sub>4</sub> in BTO results into lattice strain due to tetragonal distortion, unit cell expansion/contraction and lattice mismatch. It enhances ME coupling. The lattice distortion,  $c/a$ , tetragonal phase of BTO, spinel ferrite MFO and the lattice strain in composite phases is studied by XRD pattern [20]. These reported results also shown the AFM images to evaluate the value of average grain size for MnFO/BTO, CFO/BTO, NFO/BTO and ZFO/BTO, which is 25, 102, 24 and 133 nm, respectively. XPS analysis indicate that Fe exist into mixed +2/+3 valence states and O in both O<sup>2-</sup> and deficient states. **Figure 6(a)** shows the room temperature ferromagnetic behavior of MFO/BTO thin films by measuring ferromagnetic hysteresis (M-H<sub>dc</sub>). The measured value of saturation magnetization,  $M_s$  (kJ T<sup>-1</sup> m<sup>-3</sup>) = 1.29, 20.25, 27.64 and 6.77, remanent magnetization  $M_r$  (kJ T<sup>-1</sup> m<sup>-3</sup>) = 0.03, 3.75, 6.76 and 1.49 and with magnetic coercivity,  $H_c$  ( $\times 10^5$  Am<sup>-1</sup>) = 0.013, 0.079, 0.167 and 0.135, respectively, for MnFO/BTO, CFO/BTO, NFO/BTO and ZFO/BTO nanocomposite. An enlarged view of M-H<sub>dc</sub> as the inset of **Figure 6(a)** is also shown for more clarification. This magnetic measurement of MFO/BTO is compared with magnetization of a single phase MnFO (5.40 kJ T<sup>-1</sup> m<sup>-3</sup>), CFO (33.50 kJ T<sup>-1</sup> m<sup>-3</sup>), NFO (50.60 kJ T<sup>-1</sup> m<sup>-3</sup>) and ZFO (230 kJ T<sup>-1</sup> m<sup>-3</sup>), which indicate abrupt reduction in nanocomposite sample. This is because non-magnetic BTO phase exist in nanocomposite, which reduced the magnetization of ferrite. Since the non-magnetic elements weaken the A-B superexchange interaction which result into an increase the distance between the magnetic moments in A and B sites in spinel structure. Since the magnetization decreases/increases in ferrites is a relaxation process that might be concerned with the redistribution of oxygen vacancies reported by Wang et al. [36]. The presence of a magnetic dead or antiferromagnetic coating on the nanostructural surface have reducible value of saturation magnetization of ferrite nanoparticles [37]. Vamvakidis et al. [38] suggested that the reduction in inversion degree (~0.22) of MnFe<sub>2</sub>O<sub>4</sub> due to the partial oxidation of Mn<sup>2+</sup> to Mn<sup>3+</sup> ions results into weaker superexchange interactions between the tetrahedral and octahedral sites within the spinel structure. Bullita et al. [39] reported the cation distribution of ZnFe<sub>2</sub>O<sub>4</sub> at the nanoscale level, which is contributed by partial inverted spinel structure results into

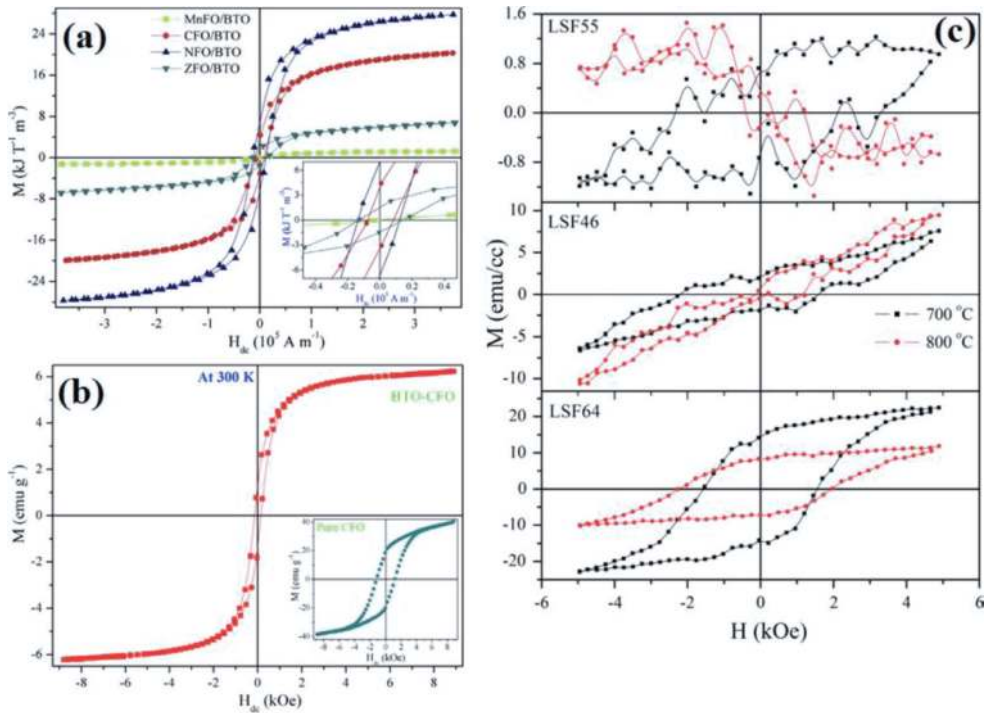


**Figure 6.** (a)  $M$ - $H_{dc}$  hysteresis of  $M\text{Fe}_2\text{O}_4/\text{BaTiO}_3$  nanocomposite thin films at 300 K. (b) Room temperature  $M$ - $H_{dc}$  measurement for pure CFO and BTO-CFO nanoparticles. (c) the  $M$ - $H$  measurement of LSF thin films. Adopted from Refs. [19, 20, 35].

an increase magnetization. Peddis et al. [40] indicates inversion degree of  $\text{CoFe}_2\text{O}_4$  nanoparticles, which has a better correlation between spin canting and cationic distribution to get competitively higher  $M_s$ .

### 3.2.5 Magnetization in CFO and 0.25BTO–0.75CFO nanoparticles

The multiferroic 0.25BTO–0.75CFO nanocomposite is prepared by hydrothermal process at 180°C/48 h [19]. The spinel CFO and tetragonal BTO structure is studied by XRD pattern. The 0.25BTO–0.75CFO nanocomposite has nanoparticles formation with average particles size from FESEM is  $80 \pm 10$  nm and from TEM is  $76 \pm 13$  nm. **Figure 6(b)** shows the  $M$ - $H_{dc}$  hysteresis for pure CFO and 0.25BTO–0.75CFO nanoparticles, measured at room temperature. The value of  $M_s$  ( $\text{emu g}^{-1}$ ) = 39.027 and 6.199,  $M_r$  ( $\text{emu g}^{-1}$ ) = 19.724 and 1.545 with  $H_c$  (Oe) = 1226 and 149, respectively, for CFO and 0.25BTO–0.75CFO nanoparticles. These measured values of  $M_s$  and  $H_c$  for pure CFO are smaller than reported for bulk  $\text{CoFe}_2\text{O}_4$  ( $M_s$  ( $\text{emu g}^{-1}$ ) = 73 and  $H_c$  (kOe) = 5, at 300 K). However, the nanocomposite of 0.25BTO–0.75CFO has abrupt decrement in  $M_s$  value, which is explained on the basis of BTO coating over CFO. For nanostructural CFO, the inversion degree must be swung with surface spin-canting and finite size-effect, to execute magnetic disorder. The change in bond angle and bond length may also influence the magnetization of CFO in composite. Since the spin coupling due to 3d unpaired electrons in  $\text{Co}^{2+}$  and  $\text{Fe}^{3+}$  along A and B-sites of spinel structure would lead to the ferrimagnetism of  $\text{CoFe}_2\text{O}_4$ . Due to such spin arrangement by unpaired electrons, there exist  $\text{Fe}_B\text{-O-Fe}_B$ ,  $\text{Fe}_B\text{-O-Co}_B$ ,  $\text{Fe}_B\text{-O-Fe}_A$ ,  $\text{Co}_B\text{-O-Fe}_A$  and  $\text{Co}_A\text{-O-Fe}_B$  superexchange interactions to induce magnetic ordering. In this, the antiferromagnetic interactions are strongest via A–O–B superexchange (inter-sublattice) and the weak ferromagnetism is attributed with A–O–A and B–O–B superexchange (intra-sublattice). It

is reported for an ideal spinel CFO, the bond angle is  $90^\circ$  of B–O–B,  $120^\circ$  of A–O–B and  $80^\circ$  of A–O–A magnetic exchange interactions. In the present case, the Rietveld analysis [19], calculated the values of bond-angle/length between A and B sites of CFO in 0.25BTO–0.75CFO nanocomposite, *i.e.*, bond angle =  $91.07^\circ$  for  $\text{Fe}_B\text{–O–Fe}_B$ ,  $133.57^\circ$  for  $\text{Fe}_A\text{–O–Co}_B$  and  $76.13^\circ$  of  $\text{Fe}_A\text{–O–Fe}_A$ . The values of bond length ( $l$ ),  $l_{A-A} = 0.3626(1)$  nm,  $l_{B-B} = 0.2961(2)$  nm and  $l_{A-B} = 0.34713(2)$  nm. It is reported that the superexchange interactions might be related with bond-angle/length among bonds in Fe, Co and O atoms [41]. For the bond angle of  $90^\circ$  ( $\text{Fe}_B\text{–O–Fe}_B$  bonds), the ferromagnetic super-exchange interaction are resulted. When this bond angle is increased, the antiferromagnetic super-exchange interactions are there and generally, bond  $120^\circ$  of super-exchange  $\text{Fe}_A\text{–O–Fe}_B$  is the dominant interaction of magnetite. Above  $120^\circ$  of bond angle, the antiferromagnetic strength is increased which is maximum at  $180^\circ$  [42]. Hence the calculated values of bond angles for Co and Fe ions along A and B-sites are deviated with theoretical one that might be indicated the distorted spinel lattice to influence resulting magnetic behavior.

### 3.2.6 Ferromagnetism in $x\text{Li}_{0.5}\text{Fe}_{2.5}\text{O}_4\text{-(1-x)}\text{SrFe}_2\text{O}_4$ thin films

The role of hard/soft ferrites composite of  $x\text{Li}_{0.5}\text{Fe}_{2.5}\text{O}_4\text{-(1-x)}\text{SrFe}_2\text{O}_4$  (LSF) ( $x = 0.4, 0.5,$  and  $0.6$ ) on the magnetic exchange-spring systems have been studied [35]. LSF thin films were prepared by MOD method. XRD result shows the polycrystalline behavior of ferrite with cubic phase of  $\text{Li}_{0.5}\text{Fe}_{2.5}\text{O}_4$  and orthorhombic  $\text{SrFe}_2\text{O}_4$ . The magnetic behavior of the three series of LSF films is investigated by measuring M–H hysteresis (**Figure 6(c)**). The Li doping into LSF enhanced the value of  $M_s$  and  $M_r$  and decreased coercivity value. At equal content of Li:Sr, the magnetic behavior is unpredictable. At annealing temperature of  $800^\circ\text{C}$ , the LSF55 thin film have anti S-type (diamagnetism), LSF64 has reducible magnetization, while LSF46 has a similar magnetism that seen at  $700^\circ\text{C}$  of annealing temperature. The values of saturation magnetization,  $M_s$  ( $\text{emu cc}^{-1}$ ) = 1.21, 8.01, and 22.78, remanent magnetization,  $M_r$  ( $\text{emu cc}^{-1}$ ) = 0.64, 2.13, and 14.20, with magnetic coercivity,  $H_c$  (kOe) = 2.32, 2.18, and 1.54, respectively, measured for LSF55, LSF46, and LSF64 sample, annealed at  $700^\circ\text{C}$ . Also from **Figure 6(c)**, the magnetic hysteresis is involved two-step processes, which might have typically exchange-spring

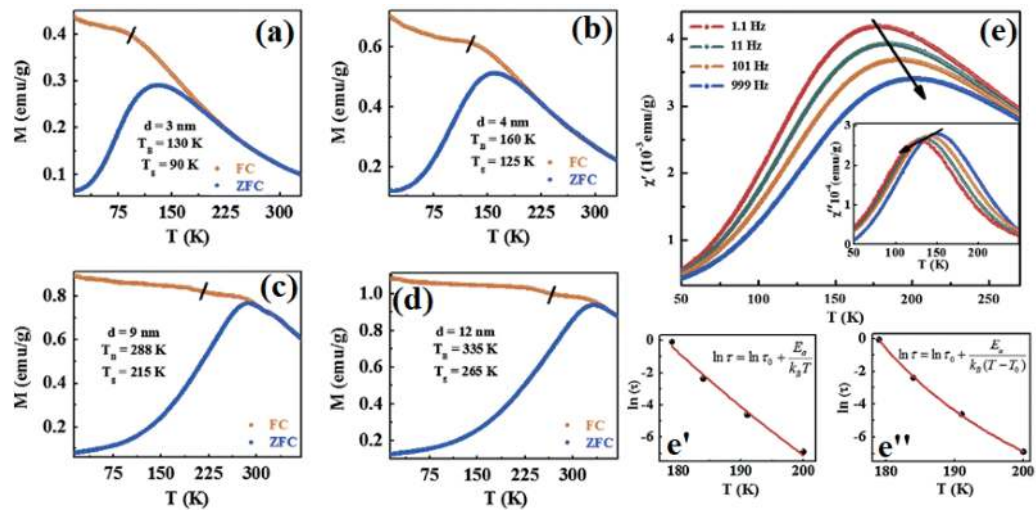


**Figure 7.** (a–d) ZFC-FC magnetization of  $\text{CoFe}_2\text{O}_4$  nanoparticles. (e) Temperature dependent  $\chi'(T)/\chi''(T)$  of ac susceptibility for  $4$  nm  $\text{CoFe}_2\text{O}_4$ . (e') Arrhenius law (e'') Vogel-Fulcher law of  $\chi'(T)$ . Adopted from Mohapatra *et al.* [45].

regime. The positive nucleation field is increased with Li doping. This positive nucleation field occurrence is predicted with a micro-magnetic model, where the perpendicular bilayer of shape anisotropy contribution is there [43].

### 3.2.7 Super-spin glass formation in CoFe<sub>2</sub>O<sub>4</sub> nanoparticles

The magnetic CoFe<sub>2</sub>O<sub>4</sub> nanoparticles of mean size 2–16 nm have been synthesized through a solventless thermolysis technique [44]. **Figure 7(a–d)** shows the ZFC/FC magnetization of 3, 4, 9 and 12 nm CoFe<sub>2</sub>O<sub>4</sub> nanoparticles in a field of 5 Oe [45]. The ZFC magnetization of these CoFe<sub>2</sub>O<sub>4</sub> nanoparticles has observed maxima, which represents the blocking temperature, T<sub>B</sub>. However, the FC magnetization is continuously increased below T<sub>B</sub>, but at a very low temperature, the FC magnetization slightly become constant. Expectedly, the FC magnetization below T<sub>B</sub> is abruptly increased with a decrease in temperature, which is because the superparamagnetic nanoparticles have no inter-particle interactions. This is typically a signature of super-spin glass transition [44]. The temperature dependent real  $\chi'$ (T) and the imaginary  $\chi''$ (T) components of the *ac* magnetic susceptibility for 4 nm CoFe<sub>2</sub>O<sub>4</sub> nanoparticles are shown in **Figure 7(e)**. The  $\chi'$ (T) curve for 1.1 Hz displays a sharp peak at the blocking temperature, T<sub>B</sub> = 179 K and the position of peak is frequency dependent. By increasing frequency from 1.1 to 999 Hz, there is shifting of peak position from 179 to 200 K that calculated the value of  $\Delta T_m = 21$  K. However,  $\chi''$ (T) in the inset of **Figure 7(e)** has also peak shifting behavior by changing peak position from 130 to 151 K with frequency 1.1–999 Hz. This is analyzed with relation:  $\phi = \Delta T_m / T_m \Delta \log(f)$ , where  $\Delta T_m$  is the difference between T<sub>m</sub> measured in  $\Delta \log(f)$  frequency interval. For non-interacting nanoparticles, this parameter ' $\phi$ ' is usually more than 0.13, for nanoparticle based superspin-glasses, the range is  $0.005 < \phi < 0.05$  and for intermediate interactions,  $0.05 < \phi < 0.13$  [46]. From **Figure 7**, the  $\phi$  values calculated to be  $\sim 0.015$ , lies for super-spin-glass systems. The super-spin glass behavior is further studied with Neel-Arrhenius law and Vogel-Fulcher model as shown in **Figure 7(e' and e'')**.

### 3.3 ZnO: diluted magnetic semiconductor

Recently, DMS ZnO has a technological potential due to its large direct band gap (3.37 eV) and exciton binding energy about 60 meV, which is comparably high [47]. The room temperature ferromagnetism, RTFM in 3d ions doped ZnO is reported by Dietl et al. [48]. But the pure ZnO is also give RTFM when the crystalline product have small sized nanoparticles [49, 50]. The oxygen vacancies are located on the nanoparticles surface and responsible in major participation of RTFM [51]. Garcia et al. [49] found that the ZnO nanoparticles had absorbed certain organic molecules to modify the electronic structure to give RTFM without any magnetic impurity. Xu et al. [50] suggested singly charged oxygen vacancies that depend upon nano-size and heating condition and located mainly near on ZnO nanoparticles surface to induce ferromagnetism. During last decade, the magnetism of ZnO with TM doping is extensively studied. Sato et al. [52] have used local density approximation (LDA) to discuss ferromagnetic ordering which is more stable in Fe-doped ZnO. Karmakar et al. [53] have found antiferromagnetism, which prefers to stabilize Fe-doped ZnO without any native defects. Spaldin [54] had found ferromagnetic ordering which is not possible when Zn sites are substituted with Co or Mn, unless additional hole carriers are incorporated. However, rare earth (RE) atoms have partially filled *f*-orbitals which carry high magnetic moments and form magnetic coupling as for TM ions with partially filled *d*-orbitals [55]. Deng et al. [56] investigated the effect of La doping on the electronic structure and optical properties of ZnO using the

first-principle calculation. It is also recently reported that the RE Ce ions are responsible in support antiferromagnetic interactions in TM = Co, Fe doped ZnO [57].

### 3.3.1 XRD for La, Gd substituted $Zn_{0.95}Co_{0.05}O$ nanostructure

The  $Zn_{0.95}Co_{0.05}O$  (ZCO5),  $Zn_{0.92}Co_{0.05}La_{0.03}O$  (ZCLO53) and  $Zn_{0.92}Co_{0.05}Gd_{0.03}O$  (ZCGO53) nanostructures were synthesized by a sol-gel process [11]. The structural information of La and Gd doped ZCO5 nanostructure using the Rietveld method for XRD pattern of wurtzite structure (space group  $P6_3mc$ ) refined and shown in **Figure 8(a)**. The miller indices of wurtzite structure (100), (002), (101), (102) and (110), respectively, observed with diffraction angle  $2\theta = 31.88, 34.49, 36.34, 47.59$  and  $49.65^\circ$  of ZnO. The XRD peak intensity of  $Zn_{0.95}Co_{0.05}O$  is reduced with La and Gd doping into it. This is because the ionic radii of  $La^{3+}$  and  $Gd^{3+}$  ions is much larger than TM  $Zn^{2+}$  and  $Co^{2+}$  ions, which results into lattice deformation of ZnO. Due to this, the lattice parameters such as lattice distortion, Zn–O bond length/angle and per unit cell volume are affected to induce lattice defects. The value of lattice constant,  $a = 3.252(1) \text{ \AA}, 3.253(2) \text{ \AA}$  and  $3.255(1) \text{ \AA}, c = 5.204(1) \text{ \AA}, 5.218(3) \text{ \AA}$  and  $5.212(3) \text{ \AA}, V = 47.660(1) \text{ \AA}^3, 47.818(3) \text{ \AA}^3$  and  $47.823(2) \text{ \AA}^3$ , and  $\chi^2 = 3.37, 0.893$  and  $2.9$ , respectively, extracted for ZCO5, ZCLO53 and ZCGO53. It is also reported that the average value of particles size,  $D$  of nano-aggregation is 142 and 86 nm, respectively, for ZCLO53 and ZCGO53 [12]. The wurtzite ZnO structure and lattice defects (vacancies/interstitials) are also found with Raman study. Photoluminescence spectra have near band edge emission (shown energy band gap,  $E_g = 3.26 \text{ eV}$  for ZCLO53 and for ZCGO53,  $E_g = 3.27 \text{ eV}$ ) and the defects/

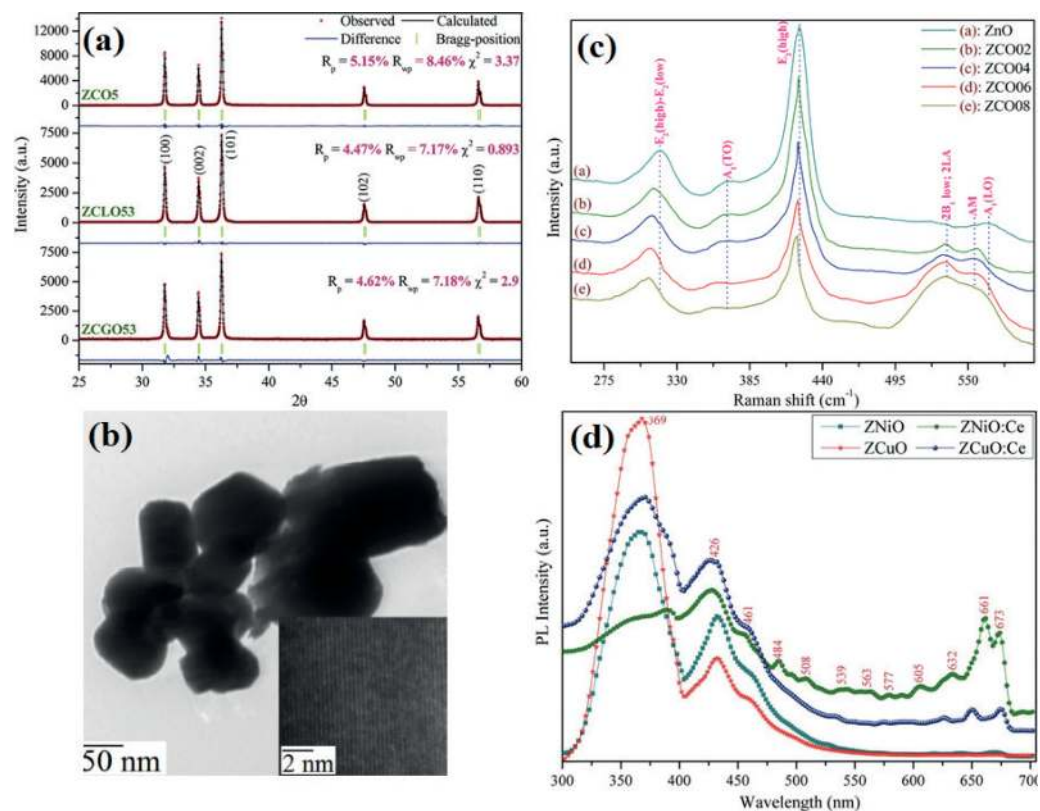


**Figure 8.** (a) XRD pattern of Co, La and Gd doped ZnO nanostructure. (b) TEM image of  $Zn_{0.94}Fe_{0.03}Ce_{0.03}O$  nanoparticles. (c) Raman spectra of pure and low Co concentrated ZnO nanoparticles. (d) Photoluminescence (PL) of Ni, Cu, Ce substituted ZnO nanoparticles. Adopted from Refs. [10, 11, 57, 58].

V<sub>O</sub> evolution with variation in visible PL spectra. The Zn<sub>0.95</sub>Co<sub>0.05</sub>O nanoparticles are paramagnetic at room temperature and involved superparamagnetic transition at low temperature. The antiferromagnetic interactions are enhanced with La and Gd doping into Zn<sub>0.95</sub>Co<sub>0.05</sub>O, is confirmed with ZFC/FC magnetization.

### 3.3.2 TEM of Zn<sub>0.94</sub>Fe<sub>0.03</sub>Ce<sub>0.03</sub>O (ZFCeO) nanoparticles

The DMS ZFCeO nanoparticles were synthesized by a sol-gel process [57]. **Figure 8(b)** shows the TEM image and the average particles size, D, of nanoparticles is  $97 \pm 4$  nm. The inset of TEM is the HRTEM to show the crystalline formation and lattice spacing after doping into ZnO. It can be noted that the distorted lattice has an enhanced interplanar spacing  $d$  [corresponding to (101) planes]  $\sim 0.247$  nm. For pure ZnO, the value of  $d \sim 0.237$  nm. In HRTEM image, some little spots that covered the lattice fringes of spacing are also observed. This is an indication towards ferromagnetic clusters or structural inclusions formation.

### 3.3.3 Raman study evaluated lattice structure inducing defects

The Zn<sub>1-x</sub>Co<sub>x</sub>O [ $x = 0.002$  (ZCO02),  $0.004$  (ZCO04),  $0.006$  (ZCO06) and  $0.008$  (ZCO08)] nanoparticles were synthesized by a sol-gel process [58]. The XRD pattern results into wurtzite ZnO structure. The ZnO with Co doping has nanorods type morphology with diameter,  $D$  (nm) =  $18 \pm 2$ ,  $23 \pm 3$ ,  $41 \pm 5$  and  $53 \pm 3$ , and length  $L$  (nm) =  $39 \pm 3$ ,  $57 \pm 5$ ,  $95 \pm 3$  and  $127 \pm 5$ , respectively, for ZCO02, ZCO04, ZCO06 and ZCO08. **Figure 8(c)** shows Raman vibrational modes, which are located at around 314, 368, 422 and 533  $\text{cm}^{-1}$  attributed to E<sub>2</sub>(high)-E<sub>2</sub>(low), A<sub>1</sub>(TO), E<sub>2</sub>(high) and (2B<sub>1</sub> low; 2LA) phonon modes, respectively [59]. The sharpest and strongest peak at about 422  $\text{cm}^{-1}$  can be attributed to nonpolar high frequency mode, E<sub>2</sub>(high), involved motion of oxygen, which is the characteristic of wurtzite lattice. With increasing Co concentration, a pronounced weakening in peak height, E<sub>2</sub>(high) mode, than pure ZnO, has been observed. The intensity of E<sub>2</sub> mode of pure ZnO is shifted towards lower frequencies with increasing Co doping. This happens because decreasing binding energy of Zn-O bonds and a tensile strain in nanograins. An additional strong peak known as additional mode (AM) is observed at 554  $\text{cm}^{-1}$  whose intensity is increased with Co concentration. This AM mode is the quasi-longitudinal optical mode formed with abundant shallow donor defects (Zn interstitial, oxygen vacancies, etc.). It is also reported in Ref. [59] that the RTFM is enhanced in low Co concentrated ZnO nanoparticles due to lattice defects. The low temperature ZFC/FC magnetic measurement indicates long-range antiferromagnetic-ferromagnetic ordering to form BMPs.

### 3.3.4 Photoluminescence spectra extract ZnO lattice defects

The Zn<sub>0.95</sub>Ni<sub>0.05</sub>O (ZNiO), Zn<sub>0.91</sub>Ni<sub>0.05</sub>Ce<sub>0.04</sub>O (ZNiO:Ce), Zn<sub>0.95</sub>Cu<sub>0.05</sub>O (ZCuO) and Zn<sub>0.91</sub>Cu<sub>0.05</sub>Ce<sub>0.04</sub>O (ZCuO:Ce) nanoparticles were synthesized by a sol-gel process [10]. **Figure 8(d)** show the PL emission for Ni, Cu, Ce substituted ZnO nanoparticles at room temperature. The peak at 369 (3.36 eV) is correlated with surface exciton recombination, which is the near band edge emission of ZnO [59]. The visible emission is formed due to radiative recombination of a photogenerated hole for which an electron occupied oxygen vacancies. The violet emission at 426 nm is the effect of radiative defects related oxygen and Zn vacancies. The peak at 461 and 484 nm is the blue emission, which have two defect level formed due to transition from Zn<sub>i</sub> to valance band or bottom of the conduction band to O interstitial. The peak at 632, 661 and 673 nm is the red emission formed with intrinsic

defect of O [60]. The Ce-doping into ZNiO and ZCuO is the production of oxygen vacancies defects in PL spectra [61].

### 3.3.5 Ferromagnetism at 300 K, 10 K of $Zn_{0.95}Ni_{0.05}O$ and $Zn_{0.91}Ni_{0.05}Ce_{0.04}O$ nanoparticles

**Figure 9** shows M-H hysteresis at 300 and 10 K, respectively, for ZNiO, ZNiO:Ce nanoparticles [10]. At 300 K, the values of  $M_s$  ( $\text{emu g}^{-1}$ ) = 0.073 and 0.085, and  $M_r$  ( $\text{emu g}^{-1}$ ) = 0.0066 and 0.0187 with  $H_c$  (Oe) = 150 and 558, respectively, for ZNiO and ZNiO:Ce. At 10 K, the value of  $M_s$  ( $\text{emu g}^{-1}$ ) = 0.096 and 0.198 and  $M_r$  ( $\text{emu g}^{-1}$ ) = 0.0129 and 0.0642 with  $H_c$  (Oe) = 76 and 165, respectively, for ZNiO and ZNiO:Ce. The RTFM in TM substituted ZnO has a great influence of the intrinsic defects such as oxygen vacancies. This is since the BMP model ascribed that the bound electrons (holes) in the defect states can couple with TM ions and cause the ferromagnetic regions to overlap, giving long range ferromagnetic ordering. A theoretical prediction based on first principle calculation in Ni-doped ZnO shows that the ferromagnetic ordering is energetically favorable through double or superexchange mechanisms [10]. The defects such as oxygen vacancies in DMS are responsible in generating carriers for ferromagnetic ordering. The observed values of  $M_s$  and  $M_r$  at 10 K, are enhanced than at room temperature. However, at low temperature ( $\sim 10$  K), the value of  $H_c$  is varies abruptly. This is due to the existence of some ferromagnetic cluster assemblies in the samples, which enlarged  $H_c$ , may an indication towards superparamagnetic/spin-glass formation [62].

### 3.3.6 FC/ZFC magnetization of $Zn_{0.95}Ni_{0.05}O$ and $Zn_{0.91}Ni_{0.05}Ce_{0.04}O$ nanoparticles

The origin of observed RTFM in Ni, Ce substituted ZnO is evaluated by the temperature dependent magnetization [ $M(T)$ ] with FC at 500 Oe and ZFC measurements (**Figure 9**) [47]. The FC/ZFC curves are separated with decrease in temperature, which usually appears with a coexistent system of antiferromagnetic and ferromagnetic phases. The steep increase of magnetization in FC curve with decreasing temperatures below 50 K is the characteristic of DMS [63]. Decreasing

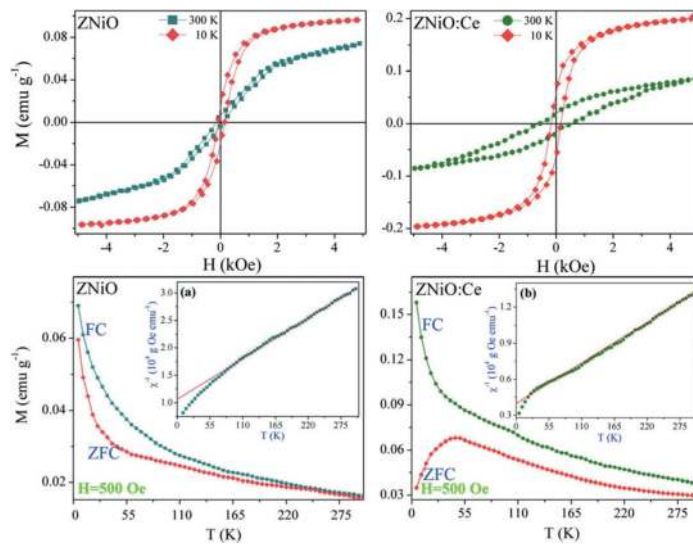


**Figure 9.** M-H hysteresis at 300 and 10 K, and  $M(T)$  measurement following FC/ZFC at  $H = 500$  Oe for ZNiO, ZNiO:Ce nanoparticles. Inset shows their  $\chi^{-1}$ - $T$  of Curie-Weiss law. Adopted from Verma and Kotnala [10].



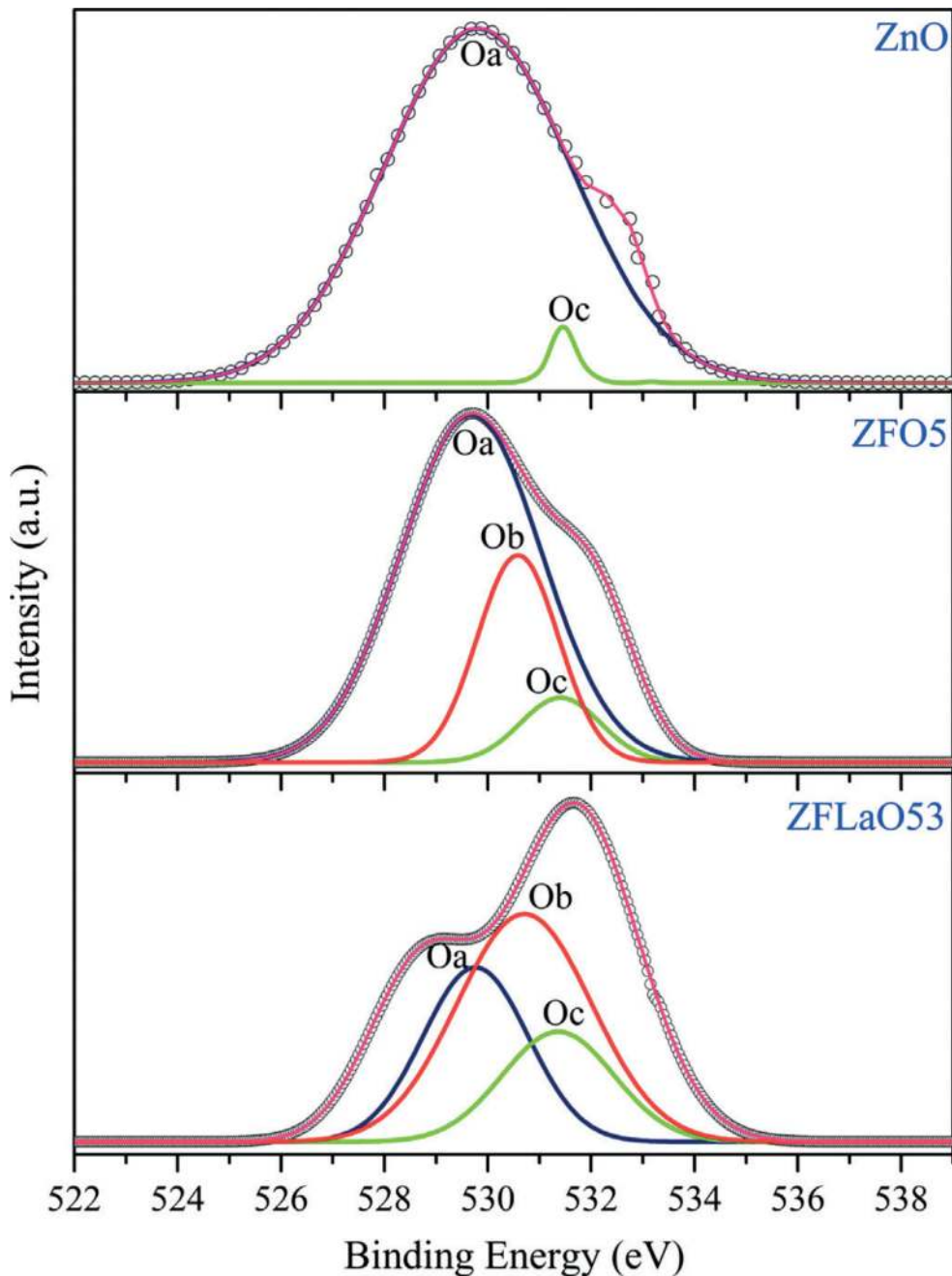


**Figure 10.**  $O\ 1s$  XPS spectra of pure  $ZnO$ ,  $Zn_{0.95}Fe_{0.05}O$  and  $Zn_{0.92}Fe_{0.05}La_{0.03}O$  nanoparticles. Adopted from Verma and Kotnala [47].

temperatures result into an increase in polarons interaction distance, leading to overlap between neighboring polarons and so allowing them to interact through the magnetic impurities, forming correlated polarons clusters. Though the direct interaction among localized carriers induced antiferromagnetism, and the ferromagnetic interaction due to BMP is possible with large magnetic impurities. When the unoccupied 3d states overlap the impurity band might be attributed high  $T_c$  value of  $ZnO$ . This is explained on the basis of donor impurity band for which oxygen vacancies involved F-centers into host  $ZnO$  [64]. The dip in ZFC curve indicates the existence of the blocking temperature,  $T_B$ . The upward curvature observed in the FC  $M(T)$  measurements (inset of **Figure 9**) of Ni and Ce substituted  $ZnO$

nanoparticles, involve a Curie–Weiss behavior related with susceptibility ( $\chi$ ) as:  $\chi = \frac{C}{T-\theta}$ ; where C is the material specific Curie constant, T is the absolute temperature, and  $\theta$  is the Weiss constant (in K) [10]. The estimated value of  $\theta$  is found to be negative, which indicate antiferromagnetic interactions. But  $\chi^{-1}(T)$  displays a notable deviation from the Curie-Weiss law that might be attributed by short-range ferromagnetism, antiferromagnetism, or a spin-glass system [65].

### 3.3.7 O 1s XPS spectra

In order to examined the presence of oxygen vacancies,  $V_O$ , the O 1s XPS spectra of pure ZnO,  $Zn_{0.95}Fe_{0.05}O$  (ZFO5) and  $Zn_{0.92}Fe_{0.05}La_{0.03}O$  (ZFLaO53) nanoparticles are given in **Figure 10** [47]. It deconvoluted into three peaks ( $O_a$ ,  $O_b$ ,  $O_c$ ). The peak located on the low binding energy side ( $O_a$ ) around 529.73 eV is attributed to  $O^{2-}$  ions on the wurtzite structure. The  $O_b$  peak at about 530.65 eV is associated with  $O^{2-}$  ions in oxygen-deficient regions within ZnO matrix, which indicate the formation of defects. The  $O_c$  peak at about 531.37 eV is usually attributed to chemisorbed oxygen on the nanostructural surface of the ZnO, such as adsorbed  $-CO_3$ ,  $H_2O$  or adsorbed  $O_2$  [66, 67].

## 4. Conclusion

The ferromagnetism in multiferroic, DMS and ferrites is a topic of intensive research due to their superficial potential in spintronic and magnetic memory devices. The lattice defects related to these multiferroic, DMS and ferrites have an important role in mediating observed ferromagnetism. The lattice defects mainly are oxygen vacancies and their formation might be related with crystalline structure, heating condition during syntheses and types of nanostructural product.

## Acknowledgements

This work is financially supported by Dr. D.S. Kothari Postdoctoral Fellowship (No.F.4-2/2006 (BSR)/PH/16-17/0066) under University Grants Commission, India.

## Author details

Kuldeep Chand Verma<sup>1\*</sup>, Ashish Sharma<sup>1</sup>, Navdeep Goyal<sup>1</sup>  
and Ravinder Kumar Kotnala<sup>2</sup>


<sup>1</sup> Department of Physics, Panjab University, Chandigarh, India

<sup>2</sup> CSIR-National Physical Laboratory, New Delhi, India

\*Address all correspondence to: [dkuldeep.physics@gmail.com](mailto:dkuldeep.physics@gmail.com)

## IntechOpen

---

© 2019 The Author(s). Licensee IntechOpen. This chapter is distributed under the terms of the Creative Commons Attribution License (<http://creativecommons.org/licenses/by/3.0>), which permits unrestricted use, distribution, and reproduction in any medium, provided the original work is properly cited. 

## References

- [1] Buurma AJC, Blake GR, Palstra TTM. Multiferroic Materials: Physics and Properties, from Encyclopedia of Materials: Science and Technology (2nd edn.), 2006. Reference Module in Materials Science and Materials Engineering. Amsterdam: Elsevier; 2016. pp. 1-7
- [2] Verma KC, Kotnala RK. Lattice defects induce multiferroic responses in Ce, La-substituted  $\text{BaFe}_{0.01}\text{Ti}_{0.99}\text{O}_3$  nanostructures. *Journal of the American Ceramic Society*. 2016;**99**:1601-1608
- [3] Bibes M, Barthelemy A. Towards a magnetoelectric memory. *Nature Materials*. 2008;**7**:425-426
- [4] Verma KC, Kotnala RK. Multiferroic approach for Cr, Mn, Fe, Co, Ni, Cu substituted  $\text{BaTiO}_3$  nanoparticles. *Materials Research Express*. 2016;**3**:055006
- [5] Verma KC, Vinay G, Kaur J, Kotnala RK. Raman spectra, photoluminescence, magnetism and magnetoelectric coupling in pure and Fe doped  $\text{BaTiO}_3$  nanostructures. *Journal of Alloys and Compounds*. 2013;**578**:5-11
- [6] Harrisa VG, Sepelak V. Mechano-chemically processed zinc ferrite nanoparticles: Evolution of structure and impact of induced cation inversion. *Journal of Magnetism and Magnetic Materials*. 2018;**465**:603-610
- [7] Sugimoto M. The past, present, and future of ferrites. *Journal of the American Ceramic Society*. 1999;**82**:269-279
- [8] Price GD, Price SL, Burdett JK. The factors influencing cation site-preferences in spinels a new mendelyevian approach. *Physics and Chemistry of Minerals*. 1982;**8**:69-76
- [9] Verma KC, Singh VP, Ram M, Shah J, Kotnala RK. Structural, microstructural and magnetic properties of  $\text{NiFe}_2\text{O}_4$ ,  $\text{CoFe}_2\text{O}_4$  and  $\text{MnFe}_2\text{O}_4$  nanoferrite thin films. *Journal of Magnetism and Magnetic Materials*. 2011;**323**:3271-3275
- [10] Verma KC, Kotnala RK. Understanding lattice defects to influence ferromagnetic order of ZnO nanoparticles by Ni, Cu, Ce ions. *Journal of Solid State Chemistry*. 2017;**246**:150-159
- [11] Verma KC, Kotnala RK. Defects due to lattice distortion and nano-size intermediate ferromagnetism in La, Gd substituted  $\text{Zn}_{0.95}\text{Co}_{0.05}\text{O}$ . *Current Applied Physics*. 2016;**16**:175-182
- [12] Kaur J, Kotnala RK, Gupta V, Verma KC. Anionic polymerization in Co and Fe doped ZnO: Nanorods, magnetism and photoactivity. *Current Applied Physics*. 2014;**14**:749-756
- [13] Prinz GA. Magnetoelectronics. *Science*. 1998;**282**:1660-1663
- [14] Verma KC, Kotnala RK. Realizing ferromagnetic ordering in  $\text{SnO}_2$  and ZnO nanostructures with Fe, Co, Ce ions. *Physical Chemistry Chemical Physics*. 2016;**18**:17565-17574
- [15] Pal B, Dhara S, Giri PK, Sarkar D. Room temperature ferromagnetism with high magnetic moment and optical properties of Co doped ZnO nanorods synthesized by a solvothermal route. *Journal of Alloys and Compounds*. 2014;**615**:378-385
- [16] McCabe GH, Fries T, Liu MT, Shapira Y, Ram-Mohan LR, Kershaw R, et al. Bound magnetic polarons in p-type  $\text{Cu}_2\text{Mn}_{0.9}\text{Zn}_{0.1}\text{SnS}_4$ . *Physical Review B*. 1997;**56**(11):6673-6680
- [17] Verma KC, Kotnala RK, Negi NS. Improved dielectric and ferromagnetic properties in Fe-doped  $\text{PbTiO}_3$  nanoparticles at room temperature.

Applied Physics Letters.  
2008;**92**:152902-152903

[18] Verma KC, Kotnala RK. Tailoring the multiferroic behavior in BiFeO<sub>3</sub> nanostructures by Pb doping. RSC Advances. 2016;**6**:57727-57738

[19] Verma KC, Singh M, Kotnala RK, Goyal N. Magnetic field control of polarization/capacitance/voltage/resistance through lattice strain in BaTiO<sub>3</sub>-CoFe<sub>2</sub>O<sub>4</sub> multiferroic nanocomposite. Journal of Magnetism and Magnetic Materials. 2019;**469**:483-493

[20] Verma KC, Singh D, Kumar S, Kotnala RK. Multiferroic effects in MFe<sub>2</sub>O<sub>4</sub>/BaTiO<sub>3</sub> (M = Mn, Co, Ni, Zn) nanocomposites. Journal of Alloys and Compounds. 2017;**709**:344-355

[21] Shen Y, Sun J, Li L, Yao Y, Zhou C, Su R, et al. The enhanced magnetodielectric interaction of (1 - x)BaTiO<sub>3</sub>-xCoFe<sub>2</sub>O<sub>4</sub> multiferroic composites. Journal of Materials Chemistry C. 2014;**2**:2545-2551

[22] Jiang K, Zhu JJ, Wu JD, Sun J, Hu ZG, Chu JH. Influences of oxygen pressure on optical properties and interband electronic transitions in multiferroic bismuth ferrite nanocrystalline films grown by pulsed laser deposition. ACS Applied Materials & Interfaces. 2011;**3**:4844-4852

[23] Li H, Huang Y, Zhang Q, Qiao Y, Gu Y, Liu J, et al. Facile synthesis of highly uniform Mn/Co-codoped ZnO nanowires: Optical, electrical, and magnetic properties. Nanoscale. 2011;**3**:654-660

[24] Kaur J, Kotnala RK, Verma KC. Multiferroic properties of Ba(Fe<sub>x</sub>Ti<sub>1-x</sub>)O<sub>3</sub> nanorods. Materials Letters. 2011;**65**:3160-3163

[25] Verma KC, Kaur J, Negi NS, Kotnala RK. Multiferroic and magnetoelectric

properties of nanostructured BaFe<sub>0.01</sub>Ti<sub>0.99</sub>O<sub>3</sub> thin films obtained under polyethylene glycol conditions. Solid State Communications. 2014;**178**:11-15

[26] Liu S, Akbashev AR, Yang X, Liu X, Li W, Zhao L, et al. Hollandites as a new class of multiferroics. Scientific Reports. 2014;**4**:6203

[27] Zhao H, Kimura H, Cheng Z, Osada M, Wang J, Wang X, et al. Large magnetoelectric coupling in magnetically short-range ordered Bi<sub>5</sub>Ti<sub>3</sub>FeO<sub>15</sub> film. SC Reports. 2014;**4**:5255

[28] Bretos I, Jimenez R, Lazaro CG, Montero I, Calzada ML. Defect-mediated ferroelectric domain depinning of polycrystalline BiFeO<sub>3</sub> multiferroic thin films. Applied Physics Letters. 2014;**104**:092905

[29] Spanier JE, Kolpak AM, Urban JJ, Grinberg I, Ouyang L, Yun WS, et al. Ferroelectric phase transition in individual single-crystalline BaTiO<sub>3</sub> nanowires. Nano Letters. 2006;**6**:735-739

[30] Beltran JJ, Barrero CA, Punnoose A. Evidence of ferromagnetic signal enhancement in Fe and Co codoped ZnO nanoparticles by increasing superficial Co<sup>3+</sup> content. Journal of Physical Chemistry C. 2014;**118**:13203-13217

[31] Li W et al. Oxygen-vacancy-induced antiferromagnetism to ferromagnetism transformation in Eu<sub>0.5</sub>Ba<sub>0.5</sub>TiO<sub>3</sub>-delta multiferroic thin films. Scientific Reports. 2013;**3**:618-616

[32] Pradhan DK, Kumari S, Puli VS, Das PT, Pradhan DK, Kumar A, et al. Correlation of dielectric, electrical and magnetic properties near the magnetic phase transition temperature of cobalt zinc ferrite. Physical Chemistry Chemical Physics. 2017;**19**:210-218

- [33] Clavel G, Marichy C, Willinger MG, Ravaine S, Zitoun D, Pinna N.  $\text{CoFe}_2\text{O}_4\text{-TiO}_2$  and  $\text{CoFe}_2\text{O}_4\text{-ZnO}$  thin film nanostructures elaborated from colloidal chemistry and atomic layer deposition. *Langmuir*. 2010;**26**(23):18400
- [34] Ahmed MA, Okasha N, Mansour SF, El-dek SI. Bi-modal improvement of the physico-chemical characteristics of PEG and  $\text{MFe}_2\text{O}_4$  subnanoferrite. *Journal of Alloys and Compounds*. 2010;**496**:345-350
- [35] Verma KC, Kotnala RK. Spring like ferromagnetic behavior of  $x\text{Li}_{0.5}\text{Fe}_{2.5}\text{O}_4-(1-x)\text{SrFe}_2\text{O}_4$  nanoferrite thin films. *Journal of Nanoparticle Research*. 2011;**13**:4437-4444
- [36] Wang P, Jin C, Zheng D, Li D, Gong J, Li P, et al. Strain and ferroelectric-field effects co-mediated magnetism in (011)- $\text{CoFe}_2\text{O}_4/\text{Pb}(\text{Mg}_{1/3}\text{Nb}_{2/3})_{0.7}\text{Ti}_{0.3}\text{O}_3$  multiferroic heterostructures. *ACS Applied Materials & Interfaces*. 2016;**8**:24198-24204
- [37] Bateer B, Tian C, Qu Y, Du S, Yang Y, Ren Z, et al. Synthesis, size and magnetic properties of controllable  $\text{MnFe}_2\text{O}_4$  nanoparticles with versatile surface functionalities. *Dalton Transactions*. 2014;**43**:9885-9891
- [38] Vamvakidis K, Katsikini M, Sakellari D, Paloura EC, Kalogirou O, Samara CD. Reducing the inversion degree of  $\text{MnFe}_2\text{O}_4$  nanoparticles through synthesis to enhance magnetization: Evaluation of their  $^1\text{H}$  NMR relaxation and heating efficiency. *Dalton Transactions*. 2014;**43**:12754-12765
- [39] Bullita S, Casu A, Casula MF, Concas G, Congiu F, Corrias A, et al.  $\text{ZnFe}_2\text{O}_4$  nanoparticles dispersed in a highly porous silica aerogel matrix: A magnetic study. *Physical Chemistry Chemical Physics*. 2014;**16**:4843-4852
- [40] Peddis D, Yaacoub N, Ferretti M, Martinelli A, Piccaluga G, Musinu A, et al. Cationic distribution and spin canting in  $\text{CoFe}_2\text{O}_4$  nanoparticles. *Journal of Physics. Condensed Matter*. 2011;**23**:426004-426008
- [41] Nedelkoski Z, Kepaptsoglou D, Lari L, Wen T, Booth RA, Oberdick SD, et al. Origin of reduced magnetization and domain formation in small magnetite nanoparticles. *Scientific Reports*. 2017;**7**:45997
- [42] Robinson DW. Magnetism and the chemical bond. In: John B, editor. Goodenough Interscience. New York: Wiley; 1963
- [43] Casoli F, Nasi L, Albertini F, Fabbri S, Bocchi C, Germini F, et al. Morphology evolution and magnetic properties improvement in FePt epitaxial films by in situ annealing after growth. *Journal of Applied Physics*. 2008;**103**:043912
- [44] Mohapatra J, Mitra A, Bahadur D, Aslam M. Surface controlled synthesis of  $\text{MFe}_2\text{O}_4$  (M = Mn, Fe, Co, Ni and Zn) nanoparticles and their magnetic characteristics. *CrystEngComm*. 2013;**15**:524-532
- [45] Mohapatra J, Mitra A, Bahadur D, Aslam M. Superspin glass behavior of self-interacting  $\text{CoFe}_2\text{O}_4$  nanoparticles. *Journal of Alloys and Compounds*. 2015;**628**:416-423
- [46] Jonsson PE. Superparamagnetism and spin glass dynamics of interacting magnetic nanoparticle systems. *Advances in Chemical Physics*. 2004;**128**:191-248
- [47] Verma KC, Kotnala RK. Oxygen vacancy induced by La and Fe into  $\text{ZnO}$  nanoparticles to modify ferromagnetic ordering. *Journal of Solid State Chemistry*. 2016;**237**:211-218

- [48] Dietl T, Ohno H, Matsukura F, Cibert J, Ferrand D. Zener model description of ferromagnetism in zinc-blende magnetic semiconductors. *Science*. 2000;**287**:1019-1022
- [49] Garcia MA, Merino JM, Pinel EF, Quesada A, dela Venta J, Ruiz Gonzalez ML, et al. Magnetic properties of ZnO nanoparticles. *Nano Letters*. 2007;**7**:1489-1492
- [50] Xu X, Xu C, Dai J, Hu J, Li F, Zhang S. Size dependence of defect-induced room temperature ferromagnetism in undoped ZnO nanoparticles. *Journal of Physical Chemistry C*. 2012;**116**:8813-8818
- [51] Gao D, Zhang Z, Fu J, Xu Y, Qi J, Xue D. Room temperature ferromagnetism of pure ZnO nanoparticles. *Journal of Applied Physics*. 2009;**105**:113928-113924
- [52] Sato K, Katayama-Yoshida H. Magnetic interactions in transition-metal-doped ZnO: An ab initio study. Ferromagnetism in a transition metal atom doped ZnO. *Physica E*. 2001;**10**:251-255
- [53] Karmakar D, Mandal SK, Kadam RM, Paulose PL, Rajarajan AK, Nath TK, et al. Ferromagnetism in Fe-doped ZnO nanocrystals: Experiment and theory. *Physical Review B*. 2007;**75**:144404-144414
- [54] Spaldin NA. Search for ferromagnetism in transition-metal-doped piezoelectric ZnO. *Physical Review B*. 2004;**69**:125201-125207
- [55] El Hachimi AG, Zaari H, Benyoussef A, El Yadari M, El Kenz A. First-principles prediction of the magnetism of 4f rare-earth-metal-doped wurtzite zinc oxide. *Journal of Rare Earths*. 2014;**32**:715-721
- [56] Deng SH, Duan MY, Xu M, He L. Effect of La doping on the electronic structure and optical properties of ZnO. *Physica B*. 2011;**406**:2314-2318
- [57] Verma KC, Kotnala RK. Defects-assisted ferromagnetism due to bound magnetic polarons in Ce into Fe, Co:ZnO nanoparticles and first-principle calculations. *Physical Chemistry Chemical Physics*. 2016;**18**:5647-5657
- [58] Verma KC, Bhatia R, Kumar S, Kotnala RK. Vacancies driven magnetic ordering in ZnO nanoparticles due to low concentrated Co ions. *Materials Research Express*. 2016;**3**:076103
- [59] Zeng H, Duan G, Li Y, Yang S, Xu X, Cai W. Blue luminescence of ZnO nanoparticles based on non-equilibrium processes: Defect origins and emission controls. *Advanced Functional Materials*. 2010;**20**:561-572
- [60] Kumar S, Basu S, Rana B, Barman A, Chatterjee S, Jha SN, et al. Structural, optical and magnetic properties of sol-gel derived ZnO:Co diluted magnetic semiconductor nanocrystals: An EXAFS study. *Journal of Materials Chemistry C*. 2014;**2**:481-495
- [61] Dar MI, Arora N, Singh NP, Sampath S, Shivashankar SA. Role of spectator ions in influencing the properties of dopant-free ZnO nanocrystals. *New Journal of Chemistry*. 2014;**38**:4783-4790
- [62] Kovaleva NN, Kugel KI, Bazhenov AV, Fursova TN, Loser W, Xu Y, et al. Formation of metallic magnetic clusters in a Kondo-lattice metal: Evidence from an optical study. *Scientific Reports*. 2012;**2**:890-897
- [63] Singhal A, Achary SN, Manjanna J, Chatterjee S, Ayyub P, Tyagi AK. Chemical synthesis and structural and magnetic properties of dispersible cobalt- and nickel-doped ZnO

Nanocrystals. *Journal of Physical Chemistry C*. 2010;**114**:3422-3430

[64] Lu ZL, Hsu HS, Tzeng YH, Zhang FM, Du YW, Huang JCA. The origins of ferromagnetism in Co-doped ZnO single crystalline films: From bound magnetic polaron to free carrier-mediated exchange interaction. *Applied Physics Letters*. 2009;**95**:102501-102503

[65] Yang CY, Lu YH, Lin WH, Lee MH, Hsu YJ, Tseng YC. Structural imperfections and attendant localized/itinerant ferromagnetism in ZnO nanoparticles. *Journal of Physics D: Applied Physics*. 2014;**47**:345003

[66] Janotti A, Van de Walle CG. Oxygen vacancies in ZnO. *Applied Physics Letters*. 2005;**87**:122102-122103

[67] Verma KC, Kotnala RK, Goyal N. *Multi-Functionality of Spintronic Materials, from Nanoelectronics Devices, Circuits and Systems*. Amsterdam, Netherlands: Elsevier; 2019. pp. 153-215